Journal of Solid State Chemistry **155,** 15–21 (2000)
doi:10.1006/jssc.2000.8882, available online at http://www.idealibrary.com on IDEAL®

Correlations between Micro- and Nanostructures and Magnetic Transitions in the Ru-Doped $Sm_{0.2}Ca_{0.8}MnO_3$ Manganites

M. Hervieu, C. Martin, A. Maignan, and B. Raveau

Laboratoire CRISMAT, UMR 6508 associé au CNRS, ISMRA et Université de Caen, 6 boulevard du Maréchal Juin, 14050 Caen Cedex, France

Received June 20, 2000; accepted July 17, 2000

DEDICATED TO PROFESSOR J. M. HONIG

The electron microscopy study of the Ru-doped manganites $Sm_{0.2}Ca_{0.8}Mn_{1-x}Ru_xO_3$ ($0 \leq x \leq 0.10$) shows that the magnetic properties of these materials are strongly correlated to their microstructure. Charge ordering induced by Mn-site doping is shown for the first time, in contrast to what is generally observed. It is shown that Ru-doping paradoxically favors the simultaneous development of ferromagnetic orthorhombic domains and charge-ordered antiferromagnetic domains at low temperature, starting from a monophasic orthorhombic paramagnetic sample at room temperature. This structural phase separation phenomenon at low temperature is explained in terms of two antagonist effects introduced by Ru^{5+} substitution: ferromagnetic superexchange interactions and Mn valency.

INTRODUCTION

The recent studies of colossal magnetoresistance (CMR) manganites have shown that several structural problems must be solved in order to understand the spectacular physical properties of these materials. It is, for instance, the case of the charge-ordering phenomena established a long time ago (1, 2), long before the discovery of CMR in those oxides (3–5). In many of these oxides, the CMR effect results from the melting of the charge-ordered state by the magnetic field, and consequently, its presence plays a very important role in the magnetotransport transitions that appear in the manganites. Another important issue concerns the electronic phase separation, involving the coexistence of regions of different carrier concentrations within the same crystal (6), which would explain the competition that appears between ferromagnetism and antiferromagnetism in manganites. Such electronic phase segregation is difficult to explain over a large-scale length and may be related to the coexistence of different structures within the same crystal. These examples clearly show that the magnetotransport properties of manganites, and especially the magnetic transitions should be clearly related to the micro- and even the nanostructure of these oxides.

The doping of Mn sites with a magnetic cation such as Cr, Ni, Co, or Ru (7–10) has shown the possibility to break the charge ordering in insulating manganites and to generate insulator-to-metal transitions, and CMR properties. Further studies of Cr-doped manganites (11, 12) have clearly established that these phenomena take place by phase separation mechanism. The recent study of the Ru-doping of the manganite $Sm_{0.2}Ca_{0.8}MnO_3$ shows that, besides the appearance of an original metal-to-metal transition, a spectacular increase of T_c up to 240 K together with CMR effect is observed (13). In the present electron microscopy study we show that the evolution of the magnetic properties of the Ru-doped $Sm_{0.2}Ca_{0.8}MnO_3$ manganites versus temperature and doping level are closely correlated to the nanostructure of these materials. Peculiar attention is focused on the charge-ordering effects induced, at low temperature, by Ru-doping in contrast to what is generally observed and expected in such oxides. These results are interpreted in terms of two factors, valency effect and ferromagnetic superexchange interactions, both due to Ru (V).

EXPERIMENTAL

The $Sm_{0.2}Ca_{0.8}Mn_{1-x}Ru_xO_3$ samples were prepared by solid state reaction at 1500°C in air, starting from the oxides Sm_2O_3, CaO, MnO_2, and RuO_2 in stoichiometric ratios. The mixtures, ground in an agate mortar, were heated at 1000°C up to a complete decarbonation. The reground powders were pressed and heated at 1500°C for 12 h. Lastly, the temperature was slowly decreased down to 800°C and the samples were quenched to room temperature.

For the electron microscopy study, small crystal flakes were deposited on a holey carbon film, supported by a copper grid. Electron diffraction (ED) study was carried out with JEOL 200CX and JEOL 2010 electron microscopes.

0022-4596/00 $35.00

Tilting around the crystallographic axes, at room temperature (RT) and 92 K, allowed reconstructing the reciprocal space. The high-resolution electron microscopy (HREM) was carried out with a TOPCON 002B microscope ($V = 200$ kV, Cs = 0.4 mm). Each of the microscopes is equipped with an energy dispersive spectroscopy (EDS) analyzer.

RESULTS

The Room Temperature Microstructure of the Series $Sm_{0.2}Ca_{0.8}Mn_{1-x}Ru_xO_3$ ($0 \leq x \leq 0.16$)

The electron diffraction study of the Ru-doped samples confirms that these oxides exhibit an orthorhombic *Pnma* structure, with $a \approx a_p\sqrt{2} \approx 5.4$ Å, $b \approx 2a_p \approx 7.7$ Å, and $c \approx a_p\sqrt{2} \approx 5.4$ Å (a_p is the parameter of a cubic perovskite subcell), exactly as for the undoped phase $Sm_{0.2}Ca_{0.8}MnO_3$ (14). Nevertheless, it must be pointed out that, beyond $x = 0.15$, structural defects are easily formed as illustrated with the ED pattern (Fig. 1a), which exhibits two systems of reflections corresponding to the perovskite and the A_3(Mn, Ru)$_2O_7$ Ruddlesden–Popper phase (labeled RP). The HREM image of such grains (Fig. 1b) shows that the defects correspond to the RP intergrowth, forming stripes that are sandwiched between *Pnma* perovskite domains.

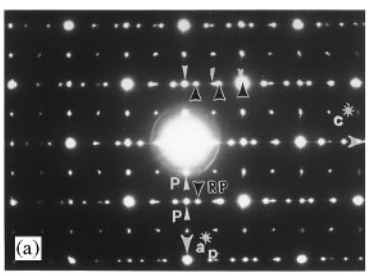

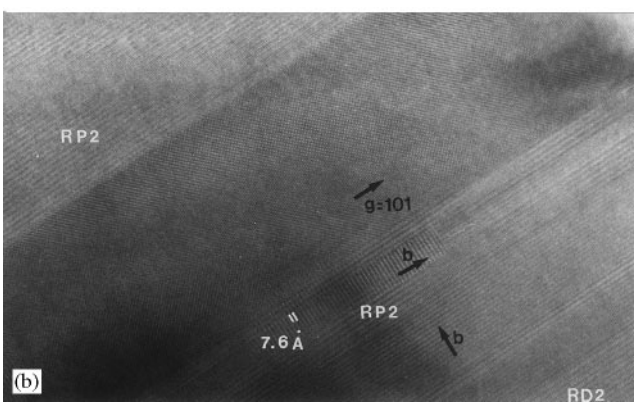

FIG. 1. Example of a defective crystal in the as-synthesized sample ($x = 0.15$). (a) ED pattern resulting from the superimposition of orthorhombic [$\bar{1}$01] and [010] domains and of $[010]_{RP}$ domains. The black arrows indicate the *h*0*l* reflections of the $m = 2$ member of the Ruddlesden–Popper family ($h + l = 2n$). The small white arrows indicate reflections of the *Pnma*-type structure. (b) Corresponding HREM image showing the sliced shape of the variants.

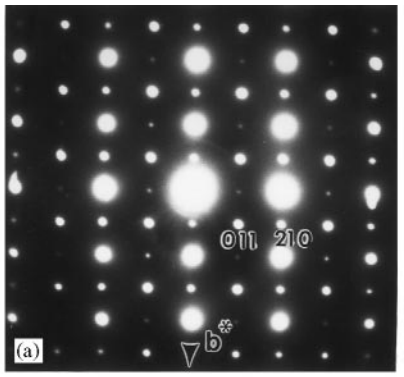

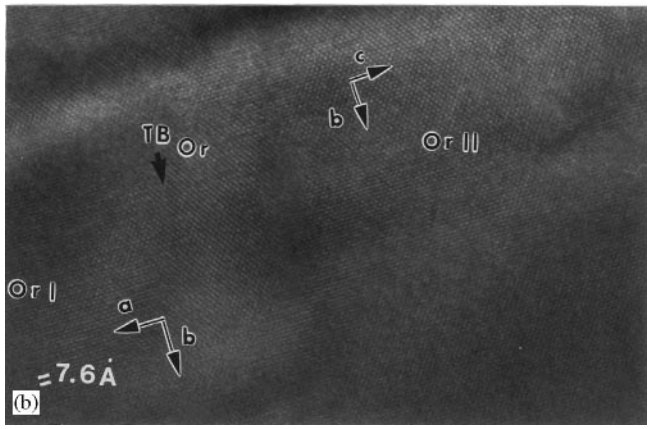

FIG. 2. (a) ED pattern and (b) HREM image of a defect free crystal (0.1 Ru content). They show the coexistence of [001]- and [100]-oriented domains with a regular contrast (denoted Or I and Or II, respectively).

Such defects can be eliminated by successive annealings at high temperature. For instance, for this $x = 0.15$ compound, a quasi-perfect orthorhombic perovskite, without RP defect, can be obtained. The HREM images of these Ru-doped perovskites show a regular contrast, which is similar to that previously observed for other CMR manganites and which is in agreement with the focus series simulated for the *Pnma*-type structures (see, for example, Ref. (15)]. One example of [100] and [010] oriented areas is given in Fig. 2. The homogeneous contrast of the through focus series evidences that the different elements, namely Ca/Sm on the one hand and Ru/Mn on the other, are randomly distributed over their respective sites of the perovskite structure.

The presence of numerous twinning domains is systematically observed in the Ru-doped compounds, exactly as in the undoped compound. These domains directly result from the orthorhombic distortion of the perovskite structure, according to the $GdFeO_3$-type structure (16); they are denoted "Or" in this paper to make the distinction with

other complex effects observed at low temperature and detailed in the next section. It must be recalled that these "Or"-type domains have been detected in all the Mn-based perovskites. The nature of the boundaries depends on the orthorhombicity of the phase, which varies with the composition, and on the presence or absence of RP defects. Figure 2 shows as an example the coexistence of two small $[100]_{or}$ and $[001]_{or}$ "Or" twinning domains and noncoherent boundaries, which appear without strain effects in the matrix. As pointed out further, homogeneity plays a very important role in the magnetotransport properties and the analysis scale must be specified carefully.

To check the homogeneity of our samples, the EDS analyses were carried out over areas of 0.01 μm^2 and several areas were measured per grain. The Ca/Sm ratio is highly constant and close to the nominal one, i.e., 4, whatever x. For the Mn/Ru ratio in the $Sm_{0.2}Ca_{0.8}Mn_{0.9}Ru_{0.1}O_3$ ($x = 0.1$) sample, the maximum and minimum observed Ru contents are 0.11 and 0.08 (these values are calculated for a total of the cations = 2). For higher Ru content ($x > 0.15$), one observes that the dispersion of the x values increases and that the average actual Ru composition is smaller than the nominal one, so that we will limit our study to $0 \leq x \leq 0.10$ for which spectacular magnetotransport properties were previously observed (13).

The Low-Temperature Microstructure of the $Sm_{0.2}Ca_{0.8}Mn_{1-x}Ru_xO_3$ Series: Correlation with the Magnetic Transitions

The magnetization curves $M(T)$ previously established (13) (Fig. 3) will serve as a guide for the exploration of the microstructure of these compounds at low temperature (92 K) by electron microscopy.

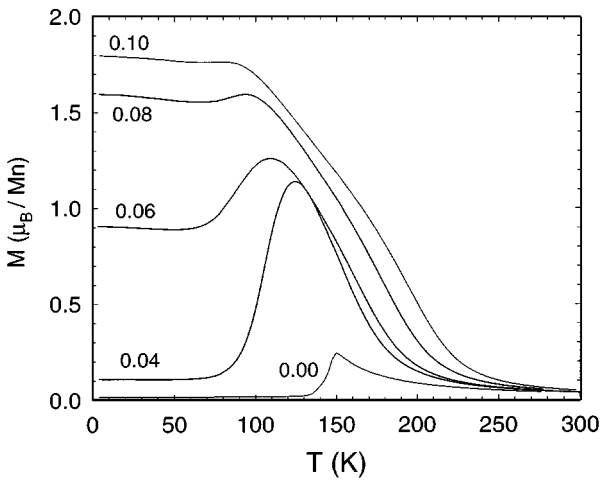

FIG. 3. Magnetization curves $M(T)$ established for $Sm_{0.2}Ca_{0.8}Mn_{1-x}Ru_xO_3$.

The Monoclinic Phase Associated to C-Type Antiferromagnetism: Low Doping Levels ($x \leq 0.04$)

For $x = 0.04$, [010] ED patterns evidence a splitting of the $h0l$ reflections at 92 K (Fig. 4a), signature of the

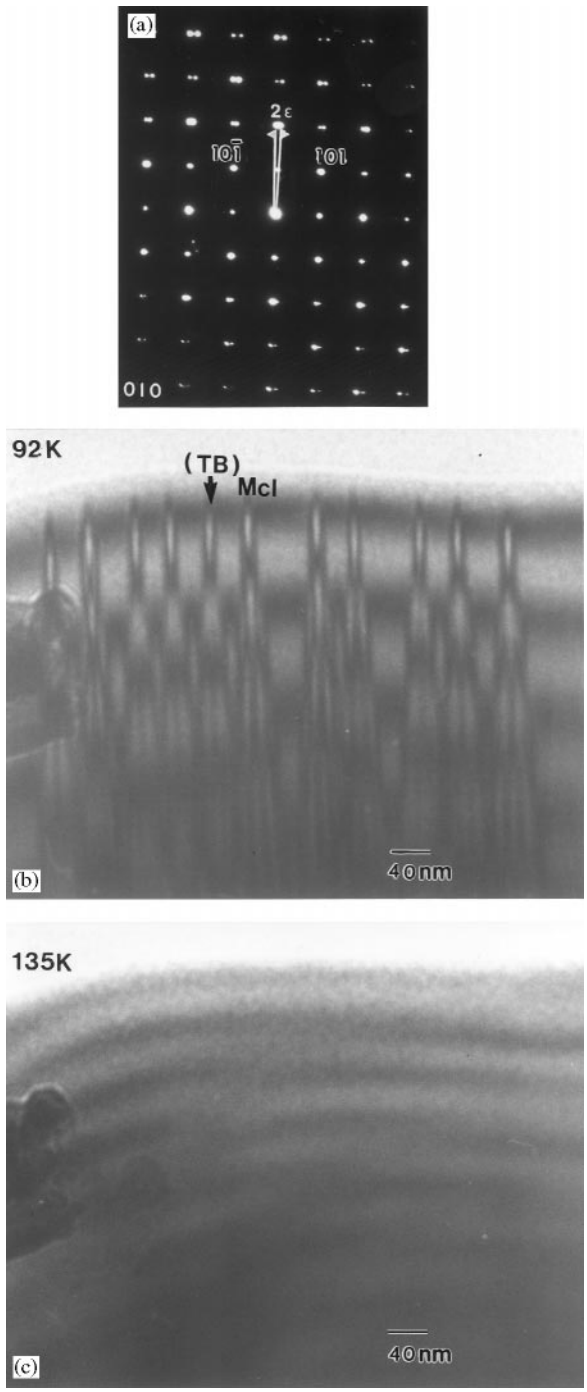

FIG. 4. $Sm_{0.2}Ca_{0.8}Mn_{0.96}Ru_{0.04}O_3$. (a) [010] ED pattern. (b) Bright field image at 92 K. $(TB)_{Mcl}$ indicates the twinning boundaries associated to the monoclinic distortion. (c) Bright field image of the area, recorded at 135 K.

monoclinic distortion of the cell, previously observed for $x = 0$ (17). The parameters of the monoclinic structure "$a_p\sqrt{2} \times 2a_p \times a_p\sqrt{2}$," with $\beta \approx (90^\circ + \varepsilon)$ and the $P2_1/m$ space group, correspond in fact to the C-type antiferromagnetic (AFM) state that has been observed at low temperature for the undoped sample by neutron diffraction (18). This observation is in agreement with the $M(T)$ curve (Fig. 3), which shows that, at this temperature, the oxide $Sm_{0.2}Ca_{0.8}Mn_{0.96}Ru_{0.04}O_3$ is antiferromagnetic. The splitting of the reflections results from the formation of twinning domains and the superposition of the two monoclinic variants with a common b^* axis. These twinning domains are denoted "Mcl" and clearly observed at 92 K in the [010] bright field images (Fig. 4b).

Warming the $x = 0.04$ sample, a very sharp transition is observed at 135 K, with an abrupt disappearance of the splitting of the reflections due to the presence of "Mcl" domains, as shown from the bright field image (Fig. 4c) recorded at 135 K. This transition temperature from the monoclinic to the orthorhombic *Pnma* symmetry coincides with the temperature of the maximum of the bump on the $M(T)$ curve (Fig. 3); a similar behavior is observed for the undoped compound but at 150 K, due to the higher Néel temperature of this phase (14). Thus, for $0 \leq x \leq 0.04$, the magnetic transition from the C-type AFM to the PM (paramagnetic) state is accompanied by a structural transition from monoclinic $P2_1/m$ to orthorhombic *Pnma*, as T increases.

It is also remarkable that the amplitude of the monoclinic distortion decreases as the Ru level, x, increases. This distortion can indeed be easily evaluated from the separation between two equivalent spots in the ED patterns. The bright field images show that concomitantly the average distance between two "Mcl"-type boundaries decreases as x increases.

The Tweed Microstructure: "Intermediate" Doping Levels ($0.06 \leq x < 0.08$)

At 92 K, for $x \approx 0.06$ the [010] ED patterns exhibit cross-shaped reflections, with more or less extended arms oriented along the two equivalent $[110]^*_p$ directions of the perovskite subcell, i.e., the [100]* and [001]* directions of the *Pnma*-type cell. The corresponding images show a net strain contrast, which is associated to a tweed structure, as shown in Fig. 5. Such a microstructure is often observed during the initial stage of a phase transition, or during the transformation of one phase into several other phases. It has been observed at room temperature in the CMR $Ln_{1-x}A_xMnO_3$ perovskite (19).

This tweed microstructure can be correlated to the $M(T)$ curve (Fig. 3), which shows that ferromagnetism (FM) has grown in the matrix, but that AFM is so far not completely destroyed (the magnetization at 92 K is only of 1.2 μ_B under 1.4T). Moreover, charge ordering is going to appear, as will be seen in the next section. Thus, this tweed microstructure certainly results from the superimposition of very tiny domains of different structural and magnetic natures in the same matrix.

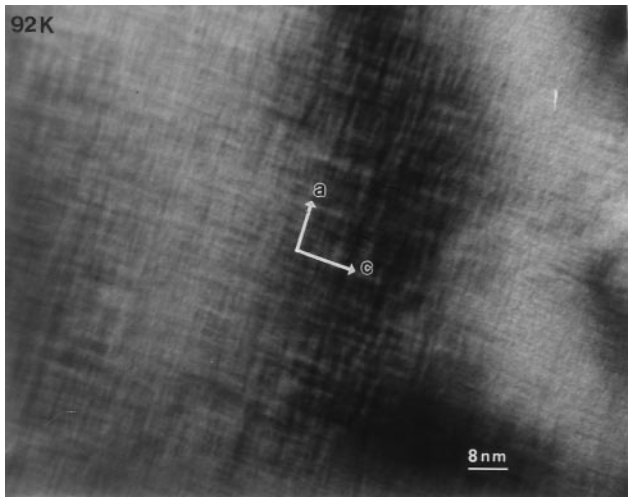

FIG. 5. [010] Bright field image of a tweed structure recorded at 92 K for $x = 0.06$.

Restoration of Charge Ordering by Ru-Doping: "Superior" Doping Levels ($x \approx 0.08$–0.10)

For $x \approx 0.08$, starting from a perfectly monophasic and homogeneous orthorhombic system at room temperature, the observations at 92 K show that a smooth structural transition and a competition between two different phases have appeared. In most of the crystallites, one observes orthorhombic *Pnma*-type domains at 92 K, similar to those observed at room temperature, which coexist with a second phase; it leads to complex ED patterns due to twinning phenomena. In a great number of ED patterns, extra satellites are observed, which involve an incommensurate superstructure along $\vec{a}^*$ with respect to the *Pnma* room temperature structure. These incommensurate modulations are characteristic of the charge ordering (CO) and have been previously characterized, using ED, in Ca-based manganites (see for example 17, 20).

For this Ru level, there is no archetype grain, but every grain is made of more or less extended and interpenetrated domains. To illustrate the microstructural state of the numerous grains that have been observed, four types of grains have been selected for the ED and lattice image observations (Figs. 6 to 9):

(i) In a number of grains, cross-shaped reflections are observed in the [010] ED patterns with elongated arms, and extra modes can be detected in few areas. One example is

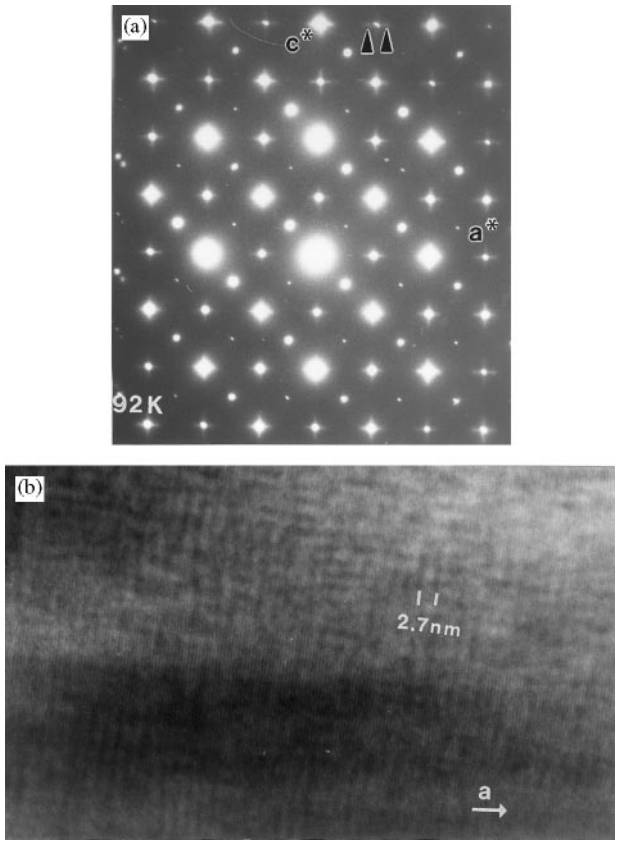

FIG. 6. [$x \approx 0.08$; $T = 92$ K]: (a) [010] ED pattern and (b) lattice image of a grain characterized by blurred fringes.

given in Fig. 6a. The value of the modulation vector q, along $\vec{a}^*$, is roughly equal to 0.18 (see small black arrows). The corresponding lattice image (Fig. 6b) shows, in the tweed structure, the formation of blurred fringes, which are not regularly spaced. These features are characteristic of the beginning of charge ordering, which tends to appear in the matrix.

(ii) For other grains, the [010] ED patterns show well-defined extra reflections (Fig. 7a). The satellites are intense and sharp. This is the signature of a quite well-established modulated structure correlated to a charge/orbital ordering phenomenon. In most of the grains, the modulation is incommensurate. The experimental q values have been observed ranging from 0.25 to 0.34, with an average value close to 0.28. The corresponding lattice image (Fig. 7b) shows a well-established system of fringes characteristic of long-range charge ordering. The bright fringes are more often spaced by $3a_p\sqrt{2}$ and $4a_p\sqrt{2}$. They are associated with the cell distortion due to the appearance of Mn^{3+} and Mn^{4+} stripes that are distributed in an incommensurate manner, in agreement with the q values measured in the ED patterns. They are similar to those observed for the charge-ordered series $Sm_{1-x}Ca_xMnO_3$ (17), for x close to 0.7. However, in the present Ru-doped manganites such an incommensurability cannot be induced by a variation of the Sm/Ca ratio, since the EDS analysis of those crystal regions confirms that the local composition remains close to the composition $Sm_{0.2}Ca_{0.8}Mn_{0.92}Ru_{0.08}O_3$.

(iii) Weak and diffuse satellites, not aligned with the a^* axis, are sometimes observed in the [010] ED patterns (see small white arrow Fig. 8a). They are associated to the formation of numerous defects in the modulated structure. The corresponding lattice image (Fig. 8b) shows indeed that the contrast of the fringes is considerably weakened and, even, no more visible in certain crystal areas where only the $a_p\sqrt{2}$ periodicity of the nonordered structure is observed. Moreover, numerous dislocation-like defects that illustrate the chaotic character of the modulation of charge-ordered state are observed (Fig. 8b). These images show the coexistence of modulated and nonmodulated areas, a few hundred nanometers large.

(iv) For several grains, the [010] ED patterns do not exhibit any satellite and are characterized by the *Pnma*

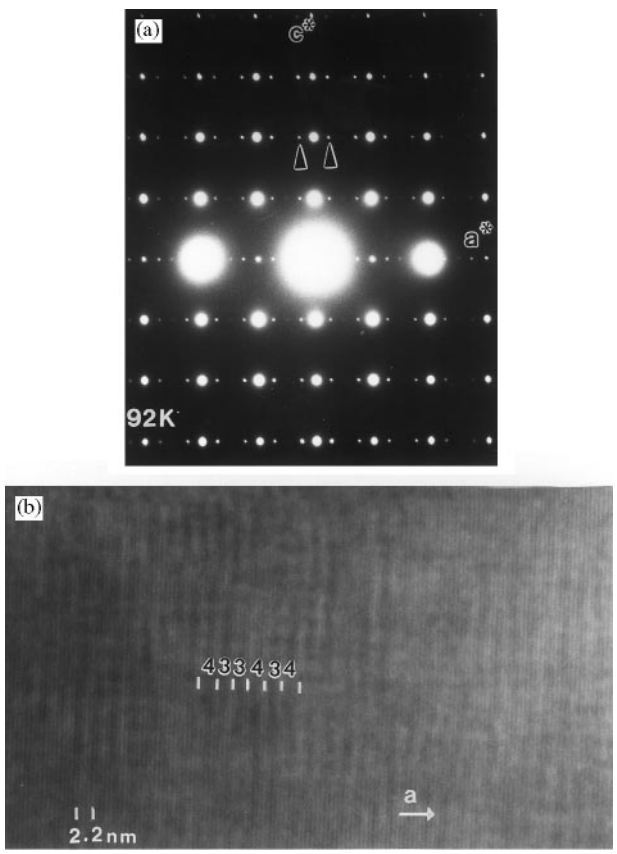

FIG. 7. [$x \approx 0.08$; $T = 92$ K]: (a) [010] ED pattern of a modulated grain. The two satellites indicated by black arrows are indexed 0021 and 002 $\bar{1}$, using four *hklm* indices. (b) Corresponding lattice image. The numbers correspond to the periodicity along $\vec{a}$ (3 and 4 times $a_p\sqrt{2}$).

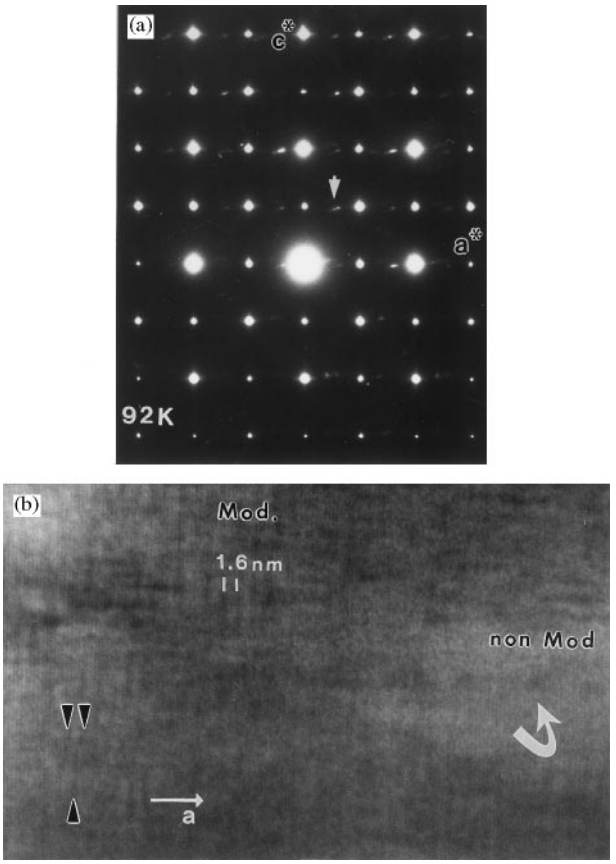

FIG. 8. [$x \approx 0.08$; $T = 92$ K]: (a) [010] ED pattern and (b) lattice image of a grain characterized by the coexistence of modulated (Mod.) and nonmodulated (non Mod.) areas, indicated by a white curved arrow. In the modulated area, numerous discommensurations are observed (see between black arrows).

structure observed at room temperature (Fig. 9a), in agreement with the corresponding lattice image (Fig. 9b).

As aforementioned, the thermal process plays an important role on the RT microstructure, depending on the nominal composition. For $x \approx 0.10$, which can be considered as the upper limit of the CO existence range, an interesting effect is observed on the LT microstructure. As an example, the low-temperature form of the as-synthesized material is orthorhombic, *Pnma* type, without neither modulation nor short-range ordering phenomena (13). On the opposite, the long- and short-range ordering effects and coexistence of two phases are clearly observed in the annealed sample. Several hypotheses can be put forward to explain such a difference in these limit compositions of competition between AFM and FM phases: small oxygen content or strain effects due to the presence of defects could be able to make appear or disappear a metastable CO. Further investigations are needed to understand this transition zone and the key parameters.

These observations show that, starting from a monophasic paramagnetic material at room temperature, structural phase separation is obtained by cooling at low temperature (92 K). Most of the grains indeed exhibit a coexistence of orthorhombic *Pnma* domains with a second structure, which either may be perfectly charge ordered or exhibits a "chaotic" modulation.

This structural behavior can be correlated to the magnetization curves (Fig. 3) which show that, for $x = 0.08$, the FM component at low temperature is significantly increased with the Ru level with respect to $x = 0.06$. The magnetic moment reaches indeed a value of 1.6 μ_B at 4.2 K (to be compared to 0.9 μ for $x = 0.06$), T_c being increased up to 220 K.

In fact, this structural phase segregation at low temperature can be explained by the appearance of two competing effects due to Ru-doping of $Sm_{0.2}Ca_{0.8}MnO_3$: ferromagnetism on one side and charge ordering on the other side. Considering the synthesis of these phases in air, it is most probable that ruthenium is pentavalent in agreement with previous results observed for ruthenium perovskites (21).

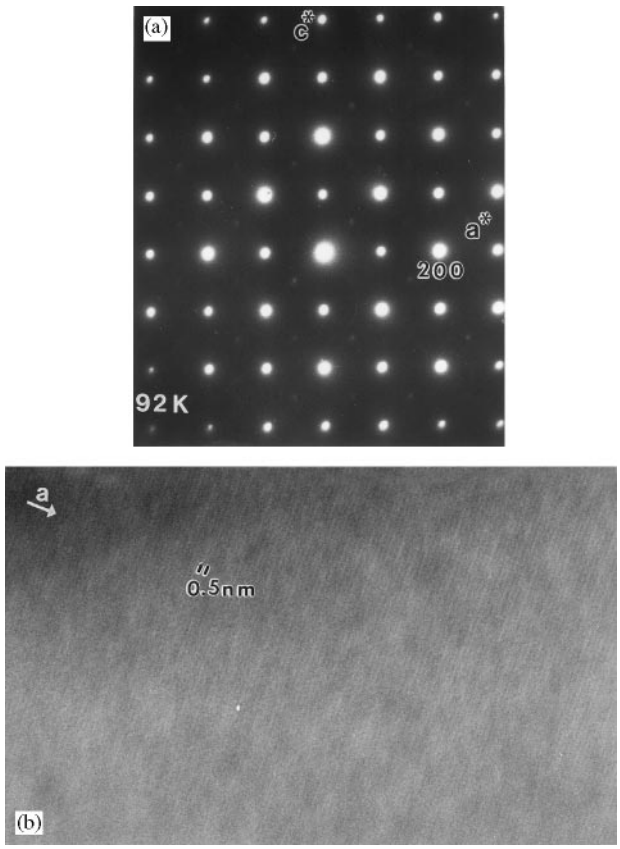

FIG. 9. [$x \approx 0.08$; $T = 92$ K]: (a) [010] ED pattern and (b) lattice image of a *Pnma*-type structure. The contrast is regular and the fringes are spaced by 5.4 Å. The weak extra reflections in the ED pattern are due to a [101] Or domain.

Then, the electronic configuration of Ru^{5+}, t_{2g}^3, similar to that of Mn^{4+}, develops strong ferromagnetic superexchange interactions with Mn^{3+} species and consequently favors the appearance of ferromagnetism. It has been previously shown that the transition from a paramagnetic to a ferromagnetic state in manganites generally occurs without any structural charge (18). Thus, the orthorhombic domains or even crystals that are observed below T_C can be attributed to the FM phase. However the pentavalent character of ruthenium induces simultaneously an antagonist effect that favors the formation of charge-ordered domains by increasing the Mn^{3+} content, according to the charge balance in the substitution reaction $2Mn^{4+} = Mn^{3+} + Ru^{5+}$. This valency effect leads indeed for $x = 0.08$ to the formula $Sm_{0.2}Ca_{0.8}Mn^{3+}_{0.28}Mn^{4+}_{0.64}Ru^{5+}_{0.08}O_3$, which shows that the Mn^{3+}/Mn^{4+} ratio is displaced toward the charge-ordered region with respect to the undoped (Sm, Ca)MnO_3 phase diagram system (17). Let us compare our $x = 0.08$ sample with the undoped manganite $Sm_{0.28}Ca_{0.72}Mn^{3+}_{0.28}Mn^{4+}_{0.72}O_3$, whose Mn^{3+} concentration with respect to the total number of sites is identical (equal to 0.28). It is remarkable that crystallites of our $x = 0.08$ sample, which exhibit rather intense satellites, show the same modulation vector $q = 0.28$ as the $Sm_{0.28}Ca_{0.72}Mn^{3+}_{0.28}Mn^{4+}_{0.72}O_3$ compound (17). This suggests that both structures are identical and consist of the same modulated distribution of Mn^{3+} stripes with Mn^{4+} or with mixed Mn^{4+}/Ru^{5+} stripes respectively. The evolution of the q vector of this $x = 0.08$ sample, versus temperature, shows that the satellites become no more detectable above 250 K, indicating that this temperature corresponds to T_{CO}. Note that this value is rather close to that previously observed for $Sm_{0.28}Ca_{0.72}MnO_3$ (17), $T_{CO} \approx 230$ K.

CONCLUSION

The electron microscopy study of the Ru-doped manganite $Sm_{0.2}Ca_{0.8}MnO_3$ shows the great tendency of this system to structural phase separation as the temperature is lowered, the microstructure of the samples and their magnetic behavior being closely correlated. Paradoxically, the Ru-doping of this manganite favors the development of ferromagnetism and charge ordering simultaneously, due to two antagonist effects of Ru^{5+} species, ferromagnetic superexchange and valency respectively. Consequently, the monoclinic $P2_1/m$ structure of the C-type AFM undoped manganite is rapidly destroyed by Ru doping at the benefit of *Pnma*, FM, and AFM structures in agreement with Ref. (22) ($x \leq 0.04$). Then, a tweed microstructure that corresponds likely to the superimposition of tiny FM and AFM domains ($x \approx 0.06$) is formed and finally orthorhombic domains, either FM or AFM, complete with charge-ordered monoclinic AFM domains ($x \sim 0.08$–0.10). These results also explain why, exceptionally, the doping of Mn-sites in this peculiar case promotes charge ordering, in contrast to what is generally observed.

REFERENCES

1. E. O. Wollan and W. C. Koehler, *Phys. Rev.* **100,** 545 (1955).
2. J. B. Goodenough, *Phys. Rev.* **100,** 564 (1955).
3. R. M. Kusters, J. Singleton, D. A. Keon, R. H. Greedy, and N. Hayes, *Physica B* **155,** 362 (1989).
4. A. Asamitsu, Y. Moritomo, Y. Tomioka, and Y. Tokura, *Nature* **373,** 407 (1995).
5. A. Maignan, Ch. Simon, V. Caignaert, and B. Raveau, *Solid State Comm.* **96,** 623 (1995).
6. S. Yunoki, J. Hu, A. Malvezzi, A. Moreo, N. Furukawa, and E. Dagotto, *Phys. Rev. Lett.* **80,** 845 (1998).
7. B. Raveau, A. Maignan, and C. Martin, *J. Solid State Chem.* **130,** 162 (1997); A. Maignan, F. Damay, C. Martin, and B. Raveau, *Mater. Res. Bull.* **32,** 965 (1997).
8. A. Barnabé, A. Maignan, M. Hervieu, F. Damay, C. Martin, and B. Raveau, *Appl. Phys. Lett.* **71,** 3907 (1997).
9. P. V. Vanitha, A. Rulraj, A. R. Raju, and C. N. R. Rao, *C. R. Acad. Sci.* **2,** 595 (1999).
10. B. Raveau, A. Maignan, C. Martin, R. Mahendiran, and M. Hervieu, *J. Solid State Chem.* **151,** 330 (2000).
11. Y. Moritomo, A. Machida, S. Mori, N. Yamamoto, and A. Nakamura, *Phys. Rev. B* **60,** 9220 (1999).
12. R. Mahendiran, M. Hervieu, A. Maignan, C. Martin, and B. Raveau, *Solid State Comm.* **114,** 429 (2000).
13. C. Martin, A. Maignan, M. Hervieu, B. Raveau, and J. Hejtmanek, *Eur. Phys. J. B* **16,** 469 (2000).
14. J. Hejtmanek, Z. Jirak, M. Marysko, C. Martin, A. Maignan, M. Hervieu, and B. Raveau, *Phys. Rev. B* **60,** 20 (1999).
15. M. Hervieu, G. Van Tendeloo, V. Caignaert, A. Maignan, and B. Raveau, *Phys. Rev. B* **53,** 14,274 (1996).
16. S. Geller and A. E. Wood, *Acta Crystallogr.* **9,** 563 (1956).
17. M. Hervieu, A. Barnabé, C. Martin, A. Maignan, F. Damay, and B. Raveau, *Eur. Phys. J. B* **8,** 31 (1999).
18. Z. Jirak, S. Krupicka, Z. Simsa, M. Dlouha, and S. Vratislav, *J. Magn. Magn. Mater.* **53,** 153 (1985); C. Martin *et al.*, submitted.
19. A. Barnabé, F. Millange, A. Maignan, M. Hervieu, and B. Raveau, *Chem. Mater.* **10,** 252 (1998).
20. C. H. Chen and S. W. Cheong, *Phys. Rev. Lett.* **76,** 4042 (1996).
21. P. D. Battle and C. W. Jones, *J. Solid State Chem.* **78,** 108 (1989); P. D. Battle, T. Gibb, C. W. Jones, and F. Studer, *J. Solid State Chem.* **78,** 281 (1989), *J. Solid State Chem.* **90,** 302 (1991).
22. C. Martin, A. Maignan, M. Hervieu, B. Raveau, Z. Jirak, M. M. Savosta, A. Kurbakov, V. Trounov, G. André, and F. Bourée, *Phys. Rev. B*, in press.